Coherent x-ray scattering

Friso van der Veen[1,2] and Franz Pfeiffer[1]

[1] Paul Scherrer Institut, CH-5232 Villigen PSI, Switzerland
[2] ETH-Zürich, Physics Department, 8093 Zürich, Switzerland

E-mail: friso.vanderveen@psi.ch and franz.pfeiffer@psi.ch

Abstract
This is a tutorial paper on the properties of partially coherent hard x-ray beams
and their use in the structural analysis of condensed matter. The role of
synchrotron radiation in the generation of coherent x-ray beams is highlighted
and the requirements on the source properties are discussed. The technique of
phase contrast imaging is briefly explained, as well as diffraction in the Fresnel
and Fraunhofer regimes. The origin of speckle is elucidated and it is shown how
oversampling of the diffraction pattern by at least a factor of two enables retrieval
of the phases of the waves scattered from different parts of the object. This in
turn allows for a direct reconstruction of the object's structure. One-dimensional
objects, such as a fluid confined between two surfaces, cannot be unambiguously
reconstructed by phase retrieval without additional assumptions. A trial-and-
error method based on the analysis of waveguiding modes within the confined
geometry is discussed.

(Some figures in this article are in colour only in the electronic version)

1. Introduction

Coherence of light is generally associated with laser-like properties. Although lasers exhibiting
multi-mode oscillations are far from ideal coherent sources, it is true that the wavefronts they
produce are highly correlated in space and time. This cannot be said about 'classical' sources
such as a lamp or a star, which spontaneously emit photons in a chaotic manner, both spatially
and temporally. Nonetheless, coherent light can be extracted from a lamp with the help of
filtering in the spatial and the temporal domains. Spatial filtering is performed by positioning
slits or pinholes along the beam path, whereas temporal filtering is achieved by extracting a
small wavelength bandwidth using a monochromator. The price to pay, of course, is a huge
loss of intensity. But if the source is sufficiently brilliant to start with, one can afford to pay
this price. Third-generation synchrotron radiation facilities are such brilliant sources. They
provide radiation ranging from the infrared to the hard x-ray regime. It is the x-ray part of the
spectrum that is of interest here.

The scattering of a fully coherent x-ray beam from an object gives rise to interference effects in the scattered beam. In the near-forward scattering direction, the phase differences between the waves traversing different parts of the object enable imaging of the object in *phase contrast*. At larger scattering angles, the interferences (the *speckle* pattern) provide us with information on its shape and internal structure on a length scale much shorter than is accessible with visible light. The retrieval of the object's real-space structure from the observed interference pattern is known as *coherent diffractive imaging* or lensless imaging, which can be regarded as holography without a reference beam.

In this tutorial paper we first introduce the physical parameters characterizing the coherence properties of electromagnetic radiation (sections 2 and 3), then we describe some applications of coherent x-ray scattering: phase contrast imaging (section 4), speckle analysis (section 5) and coherent diffractive imaging (section 7), and finally the structural analysis of confined fluids in a waveguiding geometry (section 8). A brief outlook is presented in section 9. The treatment of these subjects is kept elementary and is by no means exhaustive. For details, we refer the reader to recent papers by experts in the fields. A fundamental introduction to x-ray coherence is found in [1]. The propagation of partially coherent electromagnetic radiation is extensively treated in the classical textbooks by Born and Wolf [2] and by Goodman [3]. An excellent textbook on synchrotron x-ray physics has recently been written by Als-Nielsen and McMorrow [4]. The scattering of partially coherent x-rays by matter is treated in [5].

Time-dependent fluctuations in the speckle pattern yield insight into the structural dynamics of the object. Measuring the correlations in the arrival rate of the photons in the detector as a function of photon momentum transfer is known as *x-ray photon correlation spectroscopy (XPCS)*. It is an extension of PCS, or dynamic light scattering, in the visible [6, 7]. One may investigate the diffusion properties of complex fluids, capillary waves on surfaces, phase transitions in materials etc. This technique requires extremely brilliant beams, and hence its application is not without difficulties. XPCS will not be further discussed here. Instead we refer the reader to [8–14].

Most coherent scattering techniques that at present are implemented in the x-ray range have already been known for a long time in the visible. Apart from a 50-year time lapse, there is an amazing parallel in their development; virtually every x-ray method has its counterpart in the visible. Why then should optics be 'redone' with x-rays? There are several reasons, the most important being that x-rays are much less absorbed by matter than visible light is, so most objects are 'seen' by x-rays as *phase objects*. The relative transparency to x-rays essentially allows us to obtain an inside look into objects and to make 3D reconstructions of their internal structure. A second reason is that scattering techniques probe much smaller length scales in the x-ray range than in the visible. A third reason is that x-rays interact with matter weakly, with the result that multiple-scattering effects, which in the visible often dominate, are greatly suppressed. This helps us to extract from diffraction patterns the structure of the object.

2. Transverse coherence

Let us first consider the coherence properties of a source in a plane *transverse* to the propagation direction of the radiation. A good measure for the degree of coherence is the interference contrast recorded in the far-field diffraction pattern of an object in the beam. Let us take as an object Young's double-slit arrangement [2]. Illuminating the double slit with a monochromatic point source results in the far field in a set of interference fringes with fully developed maxima and zero intensity in the minima, corresponding to a fringe visibility of 100%.

In practice, however, the source is not point-like, but has some lateral extension. It is easy to see that this reduces the visibility of the interference fringes. Although the fringe
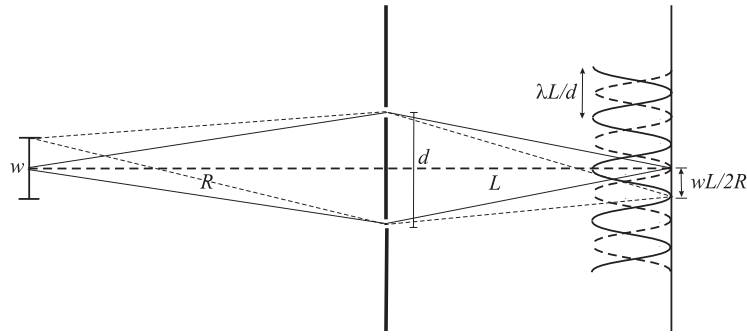
Figure 1. Diffraction patterns from two narrow slits at distance d, originating from the central part of the source (solid curve) and from the edge of the source at height $w/2$ (dashed curve). The slit distance d is such that the two patterns are in antiphase. This occurs for $d = \lambda R/w$. Angles and distances are not to scale.

patterns resulting from different points of the extended source are identical, they emerge at slightly shifted diffraction angles. Their superposition therefore causes the observed pattern to be somewhat washed out, i.e., the fringe visibility to be reduced. The effect of the extension of the source can be readily quantified. Let us consider two narrow slits at distance d, illuminated by a uniform line source of height w; see figure 1.

The interference fringes produced by an infinitesimally small emitting source element located on the optical axis appear at diffraction angles $\alpha = m\lambda/d$, with $m = 0, \pm 1, \pm 2, \dots$ for the maxima and $m = \pm\frac{1}{2}, \pm\frac{3}{2}, \pm\frac{5}{2} \dots$ for the minima. Here, the small-angle approximation has been made. The fringes produced by an emitting element at the border of the source are found at the shifted angles $m\lambda/d + w/2R$, with R the distance between the source and the slits. It is easy to see that the maxima from a border element of the source coincide with the minima from the central element at a slit separation $d = \lambda R/w$. This distance is defined as the transverse coherence length

$$\xi_t = \frac{\lambda R}{w}. \tag{1}$$

Considering now a uniform rectangular source with horizontal and vertical widths w_h and w_v, which illuminates two pairs of pinholes at right angles at distances d_h and d_v, we arrive at the corresponding transverse coherence lengths $\xi_h = \lambda R/w_h$ and $\xi_v = \lambda R/w_v$.

We stress that different elementary areas of our classic extended source independently radiate wavefronts whose amplitude and phase rapidly fluctuate in time. The influence of the source extension on any interference pattern can therefore be found by (incoherent) summation of the intensities contributed by each of the area elements over the entire source area, each contribution weighted with the intensity into the element. Synchrotron radiation sources have a Gaussian intensity distribution. The corresponding transverse coherence lengths are given by $\xi_h = \lambda R/(2\pi\sigma_h)$ and $\xi_v = \lambda R/(2\pi\sigma_v)$ [15, 16]. The limit $R \to \infty$ or $\sigma \to 0$ represents the case of a fully coherent source, characterized by an infinitely large coherence length. Third-generation synchrotron radiation sources typically have a source size of $\sigma_v \simeq 10$–$50\ \mu$m and $\sigma_h \simeq 100$–$500\ \mu$m. At a wavelength $\lambda = 0.1$ nm and at a typical distance of 40 m from the source, the transverse coherence lengths are in the ranges $\xi_v \simeq 25$–$100\ \mu$m and $\xi_h \simeq 3$–$10\ \mu$m.

How large is the photon flux through a single coherence area, i.e., through an area spanned by ξ_h and ξ_v? For simplicity we assume again that the source is uniform and rectangular with area $w_h w_v$. It has a brilliance B, which is defined as the number of photons per unit time, generated per unit source area, per unit solid angle and per 0.1% fractional bandwidth (BW)

$\Delta\lambda/\lambda$. The photon flux F transmitted by the coherence area at distance R equals

$$F = Bw_{\mathrm{h}}w_{\mathrm{v}}\Delta\Omega\frac{\Delta\lambda}{\lambda}, \tag{2}$$

with the solid angle $\Delta\Omega$ subtended by the coherence area given by $\Delta\Omega = \xi_{\mathrm{h}}\xi_{\mathrm{v}}/R^2$. Substituting the latter expression as well as the expression for the transverse coherent length, (1), in (2), we obtain

$$F = B\lambda^2\frac{\Delta\lambda}{\lambda}. \tag{3}$$

It is easy to show that (3) has the same form if the source has a Gaussian intensity distribution.

The flux through a single coherence area can now be estimated. An undulator at a third-generation source typically has a brilliance $B \sim 10^{20}$ photons s^{-1} mm^{-2} mrad^{-2} (0.1% BW)$^{-1}$. The fractional bandwidth $\Delta\lambda/\lambda$ is determined by the properties of the monochromator of the beamline at which the scattering experiment is performed. If one uses, e.g., the (111) reflection of a Si crystal monochromator, $\Delta\lambda/\lambda = 1.3 \times 10^{-4}$. At a wavelength $\lambda = 0.1$ nm, the flux through a single coherence area then equals $F = 1.3 \times 10^{11}$ photons s^{-1}. For higher fluxes one should choose a monochromator with a wider band pass such as a multilayer mirror ($\Delta\lambda/\lambda \simeq 1 \times 10^{-2}$) or just use one of the harmonics of the undulator in combination with a cut-off filter for the higher harmonics. However, there is an upper limit to the band pass, which is set by the required longitudinal coherence length; see section 3.

For the scattering to be fully coherent in the transverse directions, the object width a should be smaller than the transverse coherence length ξ_{t}. Writing (1) as $\xi_{\mathrm{t}} = \lambda/\Delta\theta$, with $\Delta\theta = w/R$, the divergence of the beam as seen at distance R from the source, we can rewrite $a < \xi_{\mathrm{t}}$ as

$$\Delta\theta < \frac{\lambda}{a}. \tag{4}$$

For a given object width, (4) sets a maximum to the allowed angular divergence.

The object may have dimensions larger than the coherence length. In that case one pre-selects a coherent beam by placing just in front of the object a small pinhole, of size $\sim\xi_{\mathrm{h}}\xi_{\mathrm{v}}$. Loosely speaking, the selected beam then has a degree of coherence close to 100%. For beam areas $A > \xi_{\mathrm{h}}\xi_{\mathrm{v}}$ the degree of coherence is correspondingly smaller.

We note that the transverse coherence length is a property of the source and the beamline optics. Young's double slit only figures as a test object [17, 18], and one may just as well take a single slit [19], a waveguide [20] or a fibre [21]. But, of course, a proper theory for the description of the partial coherence of e.m. radiation does not depend on the specific diffraction properties of an object in the beam. A rigorous treatment of the propagation of partially coherent light is found in [2].

3. Longitudinal coherence

The degree of coherence of the radiation along its propagation direction, i.e., its *longitudinal* (or temporal) coherence, enters the scattering process in a different way. Let us consider two wavefronts, one at wavelength λ and the other at a slightly different wavelength $\lambda + \Delta\lambda$, which simultaneously depart from a single point. Let us assume that after some distance ξ_{l} the two wavefronts are in antiphase; see figure 2.

If the first wave has made N oscillations over that distance, the second wave must have made $N - \frac{1}{2}$ oscillations. One therefore has $N\lambda = (N - \frac{1}{2})(\lambda + \Delta\lambda)$. Solving for N and substituting in $\xi_{\mathrm{l}} = N\lambda$ we find for this distance

$$\xi_{\mathrm{l}} \simeq \frac{1}{2}\frac{\lambda^2}{\Delta\lambda}. \tag{5}$$
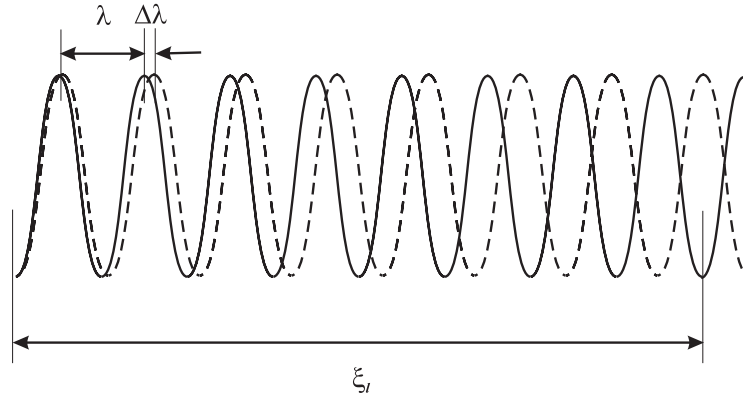
Figure 2. Propagation of two waves with wavelengths λ and $\lambda + \Delta\lambda$. The longitudinal coherence length ξ_l is defined as the distance over which the phase difference of the two waves has become π.
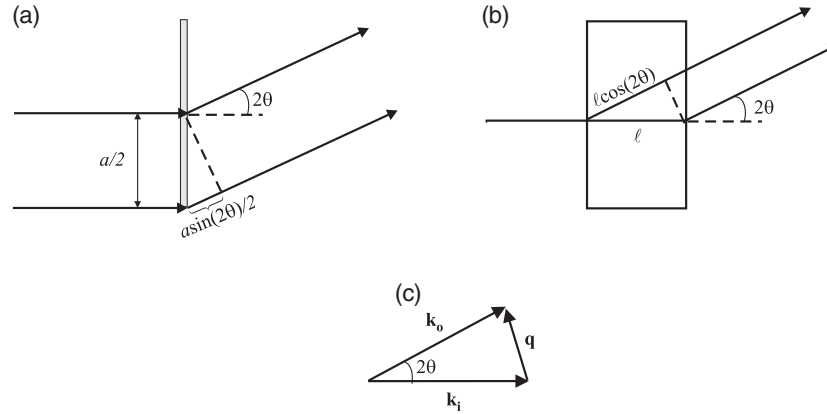

Figure 3. Scattering geometries showing the path length differences $\mathcal{PLD}$ associated with (a) the sample width a and (b) the sample thickness ℓ. Panel (c) shows the corresponding incoming and scattered wavevectors $\mathbf{k_i}$ and $\mathbf{k_o}$ and the momentum transfer $\mathbf{q}$. Angles and distances are not to scale.

The pre-factor is dependent on the spectral power density of the source; for a Lorentzian spectrum one has $\xi_l \simeq (2/\pi)\lambda^2/\Delta\lambda$ [3].

The longitudinal coherence length is inversely proportional to the bandwidth. For $\Delta\lambda/\lambda = 1.3 \times 10^{-4}$ and 0.1 nm wavelength, we find $\xi_l \simeq 400$ nm, i.e., much smaller than the transverse coherence length. In order to see the implications of a small longitudinal coherence length, consider the scattering event through an angle 2θ, from a sample having a width a and a thickness ℓ; see figure 3(a). The path length difference ($\mathcal{PLD}$) between waves scattered from the centre of the sample and from the outer edge equals $a(\sin 2\theta)/2$. A condition for coherence is that $\xi_l > \mathcal{PLD}$ or

$$\frac{\lambda^2}{\Delta\lambda} > a \sin 2\theta. \tag{6}$$

The right-hand side of this equation can be rewritten in terms of the momentum transfer $\mathbf{q} = \mathbf{k_o} - \mathbf{k_i}$, where $\mathbf{k_o}$ and $\mathbf{k_i}$ are the wavevectors of the scattered and incoming beams.

Using $|\mathbf{k_o}| = |\mathbf{k_i}| = k$, $q = 2k \sin\theta$ (figure 3(c)) and $\sin 2\theta = 2 \sin\theta \cos\theta$, we find

$$\frac{\lambda^2}{\Delta\lambda} > \frac{aq}{k}\sqrt{1 - q^2/4k^2}. \tag{7}$$

We have $q < k$, and in practice we can neglect higher-order terms in q/k:

$$\frac{\lambda^2}{\Delta\lambda} > \frac{aq}{k}. \tag{8}$$

Equation (8) must be satisfied for the largest momentum transfer q covered in the experiment, and we need sufficient momentum transfer in order to achieve a good (i.e., small) resolution. The maximum momentum transfer q_{max} relates to the spatial resolution s through $q_{max} = 2\pi/s$, and with use of $k = 2\pi/\lambda$ we can rewrite (8) as

$$\frac{\Delta\lambda}{\lambda} < \frac{s}{a}. \tag{9}$$

In order to resolve an object of size $a = 5$ μm to within $s = 10$ nm, one has to keep the fractional bandwidth $\Delta\lambda/\lambda$ below 2×10^{-3}. One then has to employ a crystal monochromator; a multilayer monochromator would not be good enough.

So far we have only considered the effect of the sample width on the $\mathcal{PLD}$. However, the sample thickness also contributes to the $\mathcal{PLD}$; see figure 3(b). The $\mathcal{PLD}$ between waves scattered from the front and the back of the sample equals $\ell(1 - \cos 2\theta) = 2\ell(\sin\theta)^2$. The condition for coherence, $\xi_l > \mathcal{PLD}$, then reads

$$\frac{\lambda^2}{\Delta\lambda} > 4\ell(\sin\theta)^2. \tag{10}$$

Of the two inequalities (6) and (10), the one whose right-hand side (rhs) is greater applies. The rhs of (10) is of order $(q/k)^2$, and the strictest requirement will almost always be (6).

For a given wavelength λ, sample width a and resolution s, the conditions for coherent scattering can be summarized as follows: equation (4) sets an upper limit on the divergence of the beam and (9) sets a limit on the fractional bandwidth.

4. Phase contrast

In this section we discuss the use of partially coherent x-ray beams for *phase contrast imaging* of objects in the limit of near-forward scattering. For the size of the structural features to be imaged, we assume that the conditions on the beamline optics, given in (4) and (9), are met.

When a coherent wavefield propagates through an object, phase differences arise between different parts of the wavefront. These are due to spatial variations in the refractive index of the object, which for x-ray wavelengths is given by

$$n = 1 - \delta + i\beta. \tag{11}$$

Here, $\beta = \mu\lambda/4\pi$ incorporates the absorption of the x-rays, with μ the absorption coefficient. This term affects the amplitude of the waves. The term

$$\delta = \lambda^2 r_e n_e/2\pi, \tag{12}$$

with $r_e = 2.818 \times 10^{-15}$ m the classical radius of the electron and n_e the electron density of the material, determines the phase of the waves and causes their refraction. For sufficiently small wavelengths ($\lambda < 0.1$ nm), β may be as small as 10^{-9}, whereas δ is of the order of 10^{-6} [22]. Phase contrast therefore dominates absorption contrast in the x-ray regime. An advantage of being sensitive to phase contrast is that even small spatial variations in the refractive index can be detected. Phase contrast x-ray imaging therefore has great potential for application
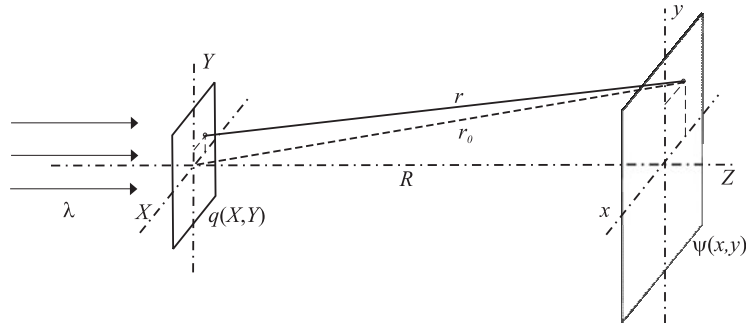
Figure 4. Propagation of a plane wave through a planar object with transmission function $q(X, Y)$. Angles and distances are not to scale.

in medicine and in biology [23], enabling one to differentiate between different kinds of soft tissue.

The structural detail in a phase contrast image depends on the distance R between the object and the detector. Three regimes for imaging can be distinguished. In the *contact* or near-contact regime, the detector is placed directly behind the object. In this case the observed contrast in the image can only be due to absorption. As one moves further away from the object, interferences build up, and one enters first the *Fresnel* diffraction regime, then the *Fraunhofer* regime [24]. In order to define these diffraction regimes, we consider a plane wave incident on a planar object with transmission function $q(X, Y)$ (see figure 4). The diffracted amplitude in the (x, y) detector plane at distance R is found by considering each infinitesimal surface element $dX\,dY$ in the object plane to be a secondary source of spherical wavelets and by summing over the total area [2]:

$$\psi(x, y) = \frac{i}{\lambda} \int \int q(X, Y) \frac{\exp(ikr)}{r} \, dX \, dY \tag{13}$$

where $r = [R^2 + (x - X)^2 + (y - Y)^2]^{1/2} = (r_0^2 - 2xX - 2yY + X^2 + Y^2)^{1/2}$ is the length of the vector connecting the point (x, y) with (X, Y). Since $\{R, r_0\} \gg \{x, X, y, Y\}$, we expand r in the exponent of (13) up to second order around r_0 and obtain

$$\psi(x, y) \simeq \frac{i \exp(ikr_0)}{\lambda r_0} \int \int q(X, Y) \exp\left(-ik\frac{xX + yY}{r_0}\right) \exp\left(ik\frac{X^2 + Y^2}{2r_0}\right) dX \, dY. \tag{14}$$

In the case of negligible absorption, the transmission function can be represented by a phase factor

$$q(X, Y) = \exp[i\phi(X, Y)], \tag{15}$$

with $\phi(X, Y)$ equal to $(2\pi/\lambda) \times$ (the optical path length difference) over the sample thickness $\ell(X, Y)$, projected onto the (X, Y)-plane:

$$\phi(X, Y) = \frac{2\pi}{\lambda} \int_0^{\ell(X,Y)} \delta(X, Y) \, dZ. \tag{16}$$

Absorption can be accounted for by replacing $\delta(X, Y)$ by $\delta(X, Y) + i\beta(X, Y)$ in the integrand of (16). If $\phi(X, Y)$ is real and small, the object is said to be a weak phase object, and one can approximate the exponent in (15) by

$$\exp[i\phi(X, Y)] \simeq 1 + i\phi(X, Y). \tag{17}$$

The exponent in the second exponential term of (14) accounts for the spherical curvature of the wavefronts. The curvature becomes negligible for $r_0 \simeq R > a^2/\lambda$, with a the sample

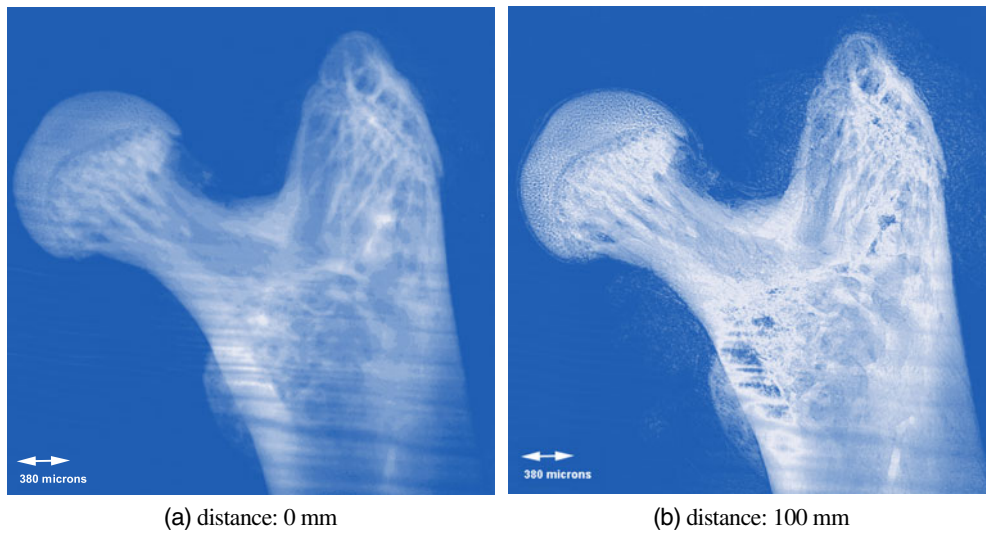(a) distance: 0 mm   (b) distance: 100 mm

Figure 5. A mouse femur head imaged at 15 keV at different sample–detector distances. From [26].

size ($a \sim \max[X, Y]$). The second exponential term then becomes unity, and the diffracted amplitude is simply the Fourier transform of $q(X, Y)$; the amplitude distribution $\psi(X, Y)$ does not change shape with increasing distance. This defines the *Fraunhofer* diffraction regime. Fresnel diffraction occurs between near-contact and the onset of the Fraunhofer diffraction regime, i.e. for $R < a^2/\lambda$ [25]. The amplitude distribution $\psi(x, y)$ may then change rapidly with distance R, because of strong interferences.

In the Fresnel diffraction regime, phase contrast can be exploited to greatest advantage. Let us consider a feature within the object plane of size ζ, at a position where the phase factor $\phi(X, Y)$ varies strongly. This feature will appear in strong phase contrast for $R < \zeta^2/\lambda$, which is the Fresnel regime for a feature of size ζ. R can now be chosen sufficiently small that only the abrupt edges of the object appear in phase contrast, while the more slowly varying structural features are still predominantly visible in absorption contrast. This choice of R leads to edge-enhanced contrast. An example is given in figure 5, which shows the image of the femur head of a mouse with the detector in near-contact (absorption contrast) and at 100 mm distance (edge-enhanced contrast) [26]. The images were taken at a wavelength of 0.08 nm. The distance is therefore such that density variations over $\zeta \simeq 3$ μm appear in enhanced contrast. Loosely speaking, figure 5(b) shows the derivative of 5(a) on that length scale.

Three-dimensional objects can be reconstructed by repeating the above imaging method for different orientations of the sample. From the corresponding family of line integrals of the form of (16), one can numerically solve for $\beta(X, Y, Z)$ and $\delta(X, Y, Z)$. This technique, which is capable of resolving structures down to a micrometre or even less, is called *computer tomography* [27].

Edge-enhanced contrast imposes only modest requirements on the source coherence. Longitudinal coherence is not an issue, because the scattering in tomography is nearly in the forward direction. The transverse coherence length only has to exceed the distance over which the density of the object changes appreciably. For an edge which extends over, say, $\zeta \simeq 3$ μm, it is sufficient that the coherence length be a few micrometres. Hence, the object plane in general contains many (10^3–10^6) coherence areas.
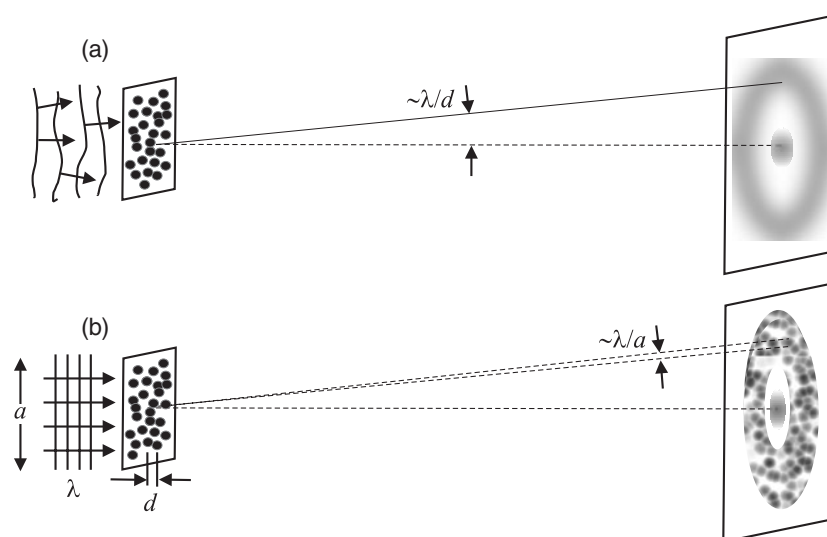
Figure 6. X-ray diffraction from a disordered medium with particle distance d. The object size is a. (a) Incoherent scattering, giving rise to a continuous diffraction ring; (b) coherent scattering, resulting in a speckled diffraction ring.

5. Speckle

Let us now assume that the object plane contains a *single* coherence area, i.e., that the scattering is fully coherent in the transverse directions. If the scattering medium is inhomogeneous, the diffraction pattern becomes speckled. This is analogous to the speckle that one sees when a laser beam is projected onto a white wall. Speckle patterns are a nuisance or a blessing, depending on the application. Clearly, in tomography one can do very well without speckle; partial coherence is only exploited in some cases to achieve edge-enhanced contrast. In addition, it is well known in optics that the imaging of an object under fully coherent illumination yields a lower spatial resolution than imaging under incoherent illumination [2]. Why then the great interest in *coherent* x-ray diffraction? This stems from the fact that one is able, in principle, to reconstruct the object's structure from the diffraction pattern in a unique way. In conventional diffraction, using an incoherent beam, this is impossible; the phases of the waves scattered from different parts of the object cannot be retrieved from the diffracted intensity pattern $|\psi(x, y)|^2$. By contrast, coherent diffraction enables us to retrieve the phases in most cases.

   X-ray speckle patterns arise in the following way [28–34]. Figure 6 compares Fraunhofer diffraction patterns taken from a disordered medium, e.g., a fluid of colloidal particles, under incoherent and coherent illumination. There are three important length scales in our problem: the wavelength λ, the average distance d between particles and the size a of the illuminated area (the particle size is left out of consideration, because it only influences the diffracted intensity distribution, not the position of the main diffraction maxima). Scale invariance implies that the pattern depends on λ/d and λ/a. But incoherent illumination cannot result in a dependence on λ/a; changing this parameter makes no difference, apart from changing the area over which the different incoherent wavefronts are averaged. The incoherent pattern therefore only depends on λ/d. Indeed, the maximum intensity is found at an angle $\sim\lambda/d$ (corresponding to the first maximum in the Patterson function [35]). The coherent diffraction pattern exhibits the same dependence, but must in addition have features of much smaller size $\sim\lambda/a$ ($\lambda/a \ll \lambda/d$, since $a \gg d$). These are the speckles.

The speckles, each having an angular width λ/a, arise from the interferences between the wavefronts scattered from the different particles. If the position of a single particle is changed, all interferences are affected, and the complete speckle pattern changes. The pattern therefore contains information on the positions of all particles, and one would like to invert the pattern in order to obtain these positions. However, it is not obvious that such an inversion can be made in a *unique* way. We will show in section 6 that a unique inversion *is* possible, provided that the features of the speckle pattern are sampled with a sufficiently high frequency.

Whereas the diffraction pattern taken under incoherent illumination is the average over patterns resulting from slightly different wavefronts and therefore resembles an average over an *ensemble* of slightly different particle configurations, the coherent pattern reflects a *particular realization* of the system. In the latter case there is no averaging over particle distances, and in fact the average distance d is irrelevant. In angle space (Fourier space) the average distance only becomes noticeable as a maximum in the envelope function of the speckles. We stress here that the speckle size λ/a is the same for all speckles and contains no information on the internal structure of the object. It is the way in which the speckles are distributed over angle and intensity that matters.

From a single speckle pattern as in figure 6(b), one can expect to obtain the object's density distribution projected onto the plane perpendicular to the beam direction. If the object is three-dimensional, one may in principle reconstruct its internal structure by taking a single speckle pattern up to very large momentum transfers (including near-backscattering). However, for a non-crystalline object this is impossible because the scattered yields are negligible at large momentum transfers. In practice one limits oneself to a rather small range of momentum transfer in the forward direction (with correspondingly lower spatial resolution) and takes a sequence of speckle patterns for different orientations of the object in the beam. This method resembles tomography, but the reconstruction algorithm is different.

6. Phase retrieval

In recent years several authors have explained why under coherent illumination, a unique determination of the density distribution within a finite-size object is possible [36–66]. Here we reproduce their arguments in a simplified form. In section 4 it was shown that the diffracted amplitude from an object in the far field is the Fourier transform of the object's transmission function $q(X, Y)$. For the sake of clarity we write (14) in a different form. For convenience we assume the object to be a one-dimensional weak phase object and obtain for the amplitude in the detector plane

$$\psi(x) \simeq \frac{i \exp(ikr_0)}{\lambda r_0} \int [1 + i\phi(X)] \exp\left(\frac{-2\pi i X x}{\lambda r_0}\right) dX, \tag{18}$$

where (17) has been used, and the second exponential factor in (14) has been set equal to unity (scattered waves are approximated by plane waves). Integration over the first term in (18) yields a delta function $\delta(x/\lambda r_0)$. This represents the direct transmitted beam, which is not considered further because it is usually blocked by a beam stop [60]. We simplify (18) further by introducing $u \equiv -x/(\lambda r_0)$, where u represents a distance in reciprocal space. It is readily verified that $u = -q/2\pi$. Replacing $\phi(X)$ in (18) by $\rho(X)$ (see (16) and (12)) and putting all constants into a single pre-factor, which is then set equal to one, we obtain

$$F(u) = \int \rho(x) \exp(2\pi i u x) \, dx. \tag{19}$$

Here, for ease of notation, we have replaced the amplitude $\psi(x)$ by the function $F(u)$ and the running variable X by x. Equation (19) simply states that the diffracted amplitude $F(u)$ is the

Fourier transform of the density $\rho(x)$. If we denote the Fourier transformation by the operator $\mathcal{F}$, (19) can be written in the shorthand notation $F(u) = \mathcal{F}[\rho(x)]$. The density $\rho(x)$ can be obtained from the diffracted amplitude through the inverse Fourier transform

$$\rho(x) = \int F(u) \exp(-2\pi \mathrm{i} u x)\, \mathrm{d}u, \tag{20}$$

which can be written as $\rho(x) = \mathcal{F}^{-1}[F(u)]$. If we were able to measure $F(u)$ directly, the density $\rho(x)$ would follow uniquely from (20). However, the detector can only measure the diffracted intensity $|F(u)|^2$, *not* the generally complex amplitude $F(u)$. Hence, phase information is lost in the measurement. In conventional crystallography, this is known as the *phase problem* [4]. Consider, for example, an infinitely long one-dimensional array of identical objects of size a and at spacing a. The corresponding density distribution can be represented by

$$\rho(x) = \rho_{\mathrm{o}}(x) \otimes \sum_{n=-\infty}^{n=\infty} \delta(x - na), \tag{21}$$

where $\rho_{\mathrm{o}}(x)$ is the density distribution within a single object, and the symbol $\otimes$ is the convolution operator defined by

$$f(x) \otimes g(x) \equiv \int_{-\infty}^{\infty} f(X) g(x - X)\, \mathrm{d}X. \tag{22}$$

Using the well-known convolution theorem of Fourier theory,

$$\mathcal{F}[f(x) \otimes g(x)] = \mathcal{F}[f(x)]\mathcal{F}[g(x)], \tag{23}$$

we find for the Fourier transform of $\rho(x)$ in (21):

$$F(u) = F_{\mathrm{o}}(u)\frac{1}{a} \sum_{m=-\infty}^{m=\infty} \delta(u - m/a). \tag{24}$$

Here, $F_{\mathrm{o}}(u) = \mathcal{F}[\rho_{\mathrm{o}}(x)]$. We conclude that diffraction from an infinite array of objects with period a results in an intensity distribution $|F(u)|^2$ given by an array of delta functions with period $1/a$ in reciprocal space (see figure 7(a)). The envelope of the intensity distribution, which determines the weight of the delta functions, is given by $|F_{\mathrm{o}}(u)|^2$. The delta functions are the Bragg peaks, and their spacing $1/a$ is the Bragg sampling interval. There is no intensity in between. Hence, for the determination of the object's structure, one only has a discrete set of values $|F_{\mathrm{o}}(m/a)|$ at one's disposal. Since the phases of $F_{\mathrm{o}}(m/a)$ have been lost, one cannot inversely transform as in (20); for this to be possible, we would need to know twice as many parameters (phases *and* amplitudes at each Bragg point) as we have measured (amplitudes only).

Now consider, instead of an infinite array of objects, a *single* object of size a, as shown in figure 7(b). Its speckled diffraction pattern is given by the continuous function $|F_{\mathrm{o}}(u)|^2$. The interval $1/a$ now arises from scattering from the top and the bottom of the single object. Sampling the diffraction pattern at half this interval, i.e. at a spacing $1/(2a)$, now enables us to solve the phase problem. This can be understood as follows. In general, the *Shannon sampling theorem* [67] states that a function $g(x)$ which is non-zero within an interval w can be fully reconstructed by sampling its Fourier transform $\mathcal{F}[g(x)]$ at a spacing $1/w$. In our case, the detector measures $\mathcal{F}[g(x)] = |F_{\mathrm{o}}(u)|^2$, and back-transforming results in

$$\begin{aligned} g(x) = \mathcal{F}^{-1}|F_{\mathrm{o}}(u)|^2 &= \mathcal{F}^{-1}[F_{\mathrm{o}}(u)F_{\mathrm{o}}^*(u)] = \mathcal{F}^{-1}[F_{\mathrm{o}}(u)] \otimes \mathcal{F}^{-1}[F_{\mathrm{o}}(u)^*] \\ &= \rho(x) \otimes \rho(-x), \end{aligned} \tag{25}$$
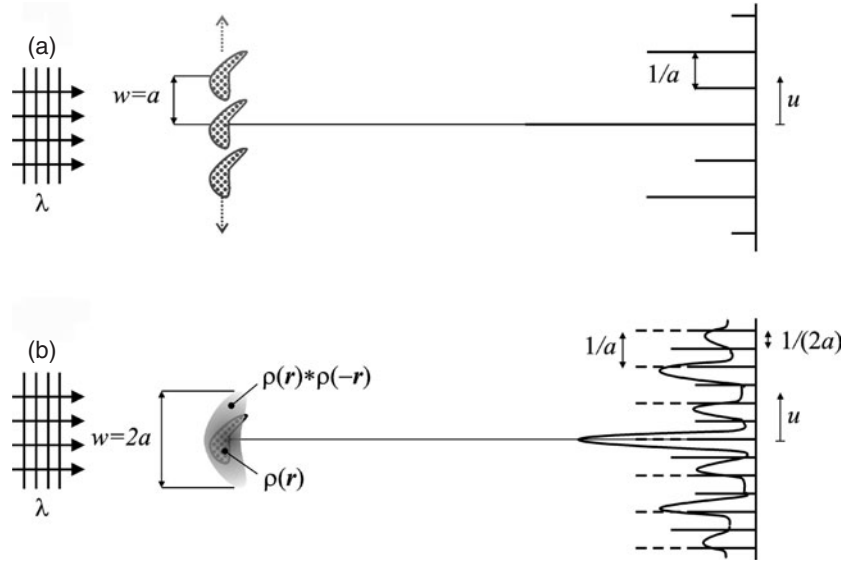
Figure 7. Coherent x-ray diffraction from an object of size a. (a) The diffraction pattern from an infinite array of objects at spacing $w = a$, giving rise to an array of sharp Bragg peaks; (b) the diffraction pattern from a single object, resulting in a continuous, speckled distribution of intensity. Sampling at the Bragg spacing $1/a$ and at the Shannon spacing $1/(2a)$ is indicated as well.

where use has been made of (20) and of the multiplication theorem of Fourier theory:

$$\mathcal{F}[f(x)g(x)] = \mathcal{F}[f(x)] \otimes \mathcal{F}[g(x)]. \tag{26}$$

The convolution $\rho(x) \otimes \rho(-x)$, which is known as the *autocorrelation function* of the density, is non-zero over an interval w equal to *twice* the object size a. In order to satisfy Shannon's theorem, one should reconstruct it by sampling its Fourier transform at a spacing $1/w = 1/(2a)$. The latter spacing represents an oversampling of the object's reciprocal space by a factor of two. In the object's real space, the sampling range corresponds to a distance of twice the object size. One knows that the object has zero density outside its boundary, and it is this knowledge that one uses to solve the phase problem.

The above statements can be cast into mathematical equations. Let the detector sample the diffraction pattern over N pixels, each having a width Δu. The corresponding real-space sampling interval equals $\Delta x = 1/(N\Delta u)$, and the position x_n of the nth sampling interval within the object is given by $x_n = n\Delta x = n/(N\Delta u)$. If the pattern is sampled at the Bragg spacing $\Delta u = 1/a$, we have $\Delta x = a/N$, and the x_n cover the entire range a in which the density $\rho(x)$ is non-zero. Discretizing the Fourier transform (19), we find for the amplitude at position $u_m = m\Delta u$ in reciprocal space:

$$|F(u_m)| = \left| \sum_{n=0}^{N-1} \rho(x_n) \exp(2\pi \mathrm{i} u_m x_n) \, \Delta x \right| = \left| \sum_{n=0}^{N-1} \rho(n\Delta x) \exp(2\pi \mathrm{i} mn/N) \, \Delta x \right|. \tag{27}$$

It is readily verified that $F(u_m)$ is a periodic function with period u_N, so

$$F(u_{N-m}) = F(-u_m). \tag{28}$$

$|F(u)|$ therefore takes maximally N different values: $|F(u_0)|, |F(u_1)|, \ldots, |F(u_{N-1})|$. If $\rho(x)$ is real (no absorption), $F^*(u) = F(-u)$ and hence $|F(u_m)| = |F(-u_m)|$. Using (28) one finds $|F(u_{N-m})| = |F(u_m)|$. In that case, only $N/2$ independent values of $|F(u_m)|$

are measured, while there are N unknown values of $\rho(x_n)$. If $\rho(x)$ is complex, we have N independent values of $|F(u_m)|$ and $2N$ unknowns $\rho(x_n)$ to be determined (the real and imaginary parts separately). In both cases, the set of equations (27) cannot be solved. Let us now oversample reciprocal space by a factor of two, i.e. we sample the diffraction pattern over $2N$ pixels, each having a width $\Delta u = 1/(2a)$. The corresponding real-space interval $\Delta x = 1/(2N\Delta u) = a/N$ and the total range of x_n remain unchanged. Equation (27) changes into

$$|F(u_m)| = \left| \sum_{n=0}^{N-1} \rho(n\Delta x) \exp\left(\frac{2\pi i m n}{2N}\right) \Delta x \right|, \tag{29}$$

with $m = 0, 1, 2, \ldots, 2N - 1$. Now there are as many unknowns as there are equations (N for $\rho(x)$ real and $2N$ for $\rho(x)$ complex), and the equations can be solved. The concept of oversampling can be brought out more clearly by rewriting (29) as

$$|F(u_m)| = \left| \sum_{n=0}^{2N-1} \rho(n\Delta x) \exp\left(\frac{2\pi i m n}{2N}\right) \Delta x \right|, \tag{30}$$

with

$$\rho(x_n) = 0 \qquad \text{for } N \leqslant n \leqslant 2N - 1 \tag{31}$$

and $m = 0, 1, 2, \ldots, 2N - 1$. The advantage of this notation is that there are as many sampling intervals in real space as there are in reciprocal space, allowing discrete Fourier transform algorithms to be readily applied.

For one dimension, the equations (29) generally have more than one solution [68], but for higher dimensions (2D or 3D) they usually have a unique solution. The above equations can readily be generalized to higher dimensions by introducing the vectors $\mathbf{r}$ and $\mathbf{u}$ for the real-space and reciprocal-space coordinates and by rewriting (19) as

$$F(\mathbf{u}) = \int \rho(\mathbf{r}) \cdot \exp(2\pi i \mathbf{u} \cdot \mathbf{r}) \, d^3\mathbf{r}. \tag{32}$$

In discretized form, the three-dimensional analogue of (29) is

$$
\begin{aligned}
|F(\mathbf{u}_m)| &= \left| \sum_{n=0}^{N^3-1} \rho(\mathbf{r}_n) \cdot \exp(2\pi i \mathbf{u}_m \cdot \mathbf{r}_n) \, \Delta^3\mathbf{r} \right| \\
&= \left| \sum_{n_x=0}^{N-1} \sum_{n_y=0}^{N-1} \sum_{n_z=0}^{N-1} \rho(n_x\Delta x, \, n_y\Delta y, \, n_z\Delta z) \right. \\
&\quad \times \left. \exp\left[\frac{2\pi i(m_x n_x + m_y n_y + m_z n_z)}{2^{3/2} N}\right] \Delta x \Delta y \Delta z \right|.
\end{aligned}
\tag{33}
$$

Here we assume along each axis an oversampling interval $\Delta u_x = 1/(2^{3/2}a_x)$, $\Delta u_y = 1/(2^{3/2}a_y)$ and $\Delta u_z = 1/(2^{3/2}a_z)$, where a_x, a_y and a_z are the object's dimensions along the x-, y- and z-axes. The corresponding real-space intervals are $\Delta x = a_x/N$, $\Delta y = a_y/N$ and $\Delta z = a_z/N$. Note that the oversampling by a factor of two refers to three-dimensional space, not to each dimension separately [44]. In this example, we took for each of the three directions the same oversampling ratio of $2^{3/2}$, but, with some restrictions, these ratios may also be chosen different. One can bring (33) into the same form as (30), on the condition that the density is padded with zeros outside the object region. An oversampling ratio larger than two, which implies a larger no-density region, renders the set of equations (33) overdetermined, which results in a more accurate reconstruction. In order to achieve low-noise reconstructions,
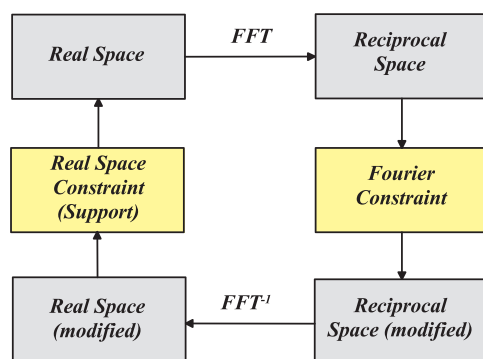
Figure 8. A schematic representation of the Gerchberg–Saxton algorithm [37]. One iterates between real space and reciprocal space using the fast Fourier transform (FFT) and its inverse and imposes known constraints in both spaces (see the text).

oversampling ratios substantially larger than two (e.g., 4 or 5) should be chosen. Equation (33) can be readily modified so as to apply to reconstruction of a 2D object.

We note again that one usually reconstructs a 3D phase object by rotating it in the beam through 180° and recording an oversampled 2D diffraction pattern at each rotation angle [60]. The 2D patterns are then assembled to a 3D diffraction pattern. Here the meaning of N^3 is not the physical number of detector pixels as stated before, but instead the number of pixels generated by the detector *and* by the number of rotation steps.

The density is reconstructed from the 3D diffraction pattern using the equations given in (33). Usually these equations are not directly solved, but an iterative procedure known as the Gerchberg–Saxton algorithm is applied [37]. At the heart of the algorithm is the fact that oversampling in reciprocal space implies sampling the object's density in parts of real space where it is known to be zero. One therefore has to have *a priori* knowledge of the object's size, for which one may take half the width of the 3D density autocorrelation function $\rho(\mathbf{r}) \otimes \rho(-\mathbf{r})$. One defines a *support* region, in which the density is allowed to be non-zero, and an outside region, in which the density is padded with zeros. The oversampling ratio is simply given by the ratio of the total sampling area in real space to the support area. The algorithm then proceeds as shown schematically in figure 8. One begins by assigning a set of random phases to the support (assuming zero absorption). Fast Fourier transformation (FFT) yields a diffraction pattern that differs from the measured one. After replacing the calculated values $|F(\mathbf{u}_m)|$ by the measured ones, one performs an inverse transformation (FFT^{-1}) and obtains a complex density distribution in real space which generally is non-zero outside the support. One puts the density to zero outside the support and requires it to be real and positive inside, and one Fourier transforms again. This cycle is repeated until convergence is achieved, i.e., until the constraints in real and reciprocal space are both fulfilled within a certain error margin.

Scattering phases may also be retrieved by completely different methods, which operate in the Fresnel diffraction regime. Cloetens *et al* [69] take a sequence of Fresnel diffraction patterns at various distances from the object. This makes each pattern sensitive to a different spatial frequency (see section 4). Analysing the sequence using a method derived from high-resolution electron microscopy [71], one obtains a 2D map of the gradient of the phase and thus of the density gradient. 3D maps are then constructed by repeating the mapping for different rotation angles of the sample. The method does not assume knowledge of the object boundary, but does require a large data set. Nugent *et al* [70] developed a quantitative phase imaging method, which is based on a single Fresnel pattern at fixed distance and on use of the so-called

transport of intensity equation [72]. Since not all spatial frequencies are probed, one may miss specific structural details. For a discussion of these interesting developments we refer the reader to the relevant literature.

7. Diffractive imaging

The method explained in section 6 can be used for the imaging of objects, crystalline or non-crystalline [73, 56, 53, 64]. The imaging does not require a lens, and reconstruction of the object is entirely based on retrieval of the scattering phases.

A beautiful example of object reconstruction is found in figure 9 taken from [61]. A 2D diffraction pattern ($\lambda = 2$ Å) from a micro-sized gold structure on a silicon nitride membrane was phased using the Gerchberg–Saxton algorithm. The reconstruction reproduced the electron microscopy image, and a spatial resolution of 7 nm was achieved. An oversampling ratio of 5 reduced noise and prevented trapping of the numerical algorithm in a local minimum.

The oversampling technique can also be used for the imaging of nanocrystals [64, 74]. Figure 10 shows a continuous diffraction pattern from a single nanocube around one of the Bragg peaks associated with diffraction from its internal lattice planes. A 3D pattern is collected by rocking the crystal around the Bragg angle under consideration, so that a series of 2D projections perpendicular to the Bragg-scattered wavevector $\mathbf{k_f}$ is obtained. Figure 10(a) illustrates this using a Ewald construction where, instead of the crystal, the Ewald sphere is rotated around the origin of reciprocal space. Reconstruction of the crystal from the continuous pattern around the (hkl) reflection yields the electron density distribution within the crystal giving rise to that reflection. In this way, dislocation bands or other structural defects within the nanocrystal can be made directly visible. Figure 10(d) shows a reconstruction based on the Gerchberg–Saxton algorithm in a 2D projection, obtained from the pattern in figure 10(c). Note that for a complete series of 2D projections only a small angular range is required, since most of the momentum is transferred via the fixed reciprocal-lattice vector $\mathbf{G}_{hkl}$. By contrast, the forward scattering geometry, which was previously discussed, requires rotation of the sample over 180° for a complete recording of the 3D pattern. But of course, the Bragg scattering geometry differs from the forward scattering geometry in that one filters out the component of the density distribution that contains the spatial frequency $1/G_{hkl}$. As a result, it is only of use for the imaging of small crystalline objects. When it *can* be used, it has the additional advantages that a stop for the direct beam is not required and that one does not have to deal with diffraction features from the pinhole in front of the sample.

The period of fringes seen in the diffraction pattern of figure 10(c) corresponds to a spatial frequency of $1/a$, with a the distance between two opposing faces of a single nanocube. One may interpret these fringes as speckles, but they differ from those shown, e.g., in figure 6(b) or figure 9(b). Whereas regular fringes arise from the well-defined *edges* of a single nanocube, the speckle distributions of figure 6(b) and of figure 9(b) arise from interferences between waves scattered from different (irregular) *internal* parts of the object, be it a collection of particles or a collection of objects, as shown in figure 9(a). But in all cases, by its very nature, the speckle width is the reciprocal of the beam width. In the Bragg geometry of figure 10, the beam width equals the object width; in the forward scattering geometry or in specular reflection geometry, it is given by the size of the pinhole.

The necessity of oversampling the diffraction patterns results in a stricter requirement on the beam divergence than that formulated in (4). Sampling at the Shannon spacing $\Delta u = 1/(2a)$ corresponds to an angular pixel size of $\Delta\alpha = \lambda/(2a)$, which the detector must resolve. Of course, the angular divergence $\Delta\theta$ of the incident beam must be smaller than $\Delta\alpha$. This then implies that (4) must be replaced by $\Delta\theta < \lambda/(2a)$. Usually, the oversampling ratio
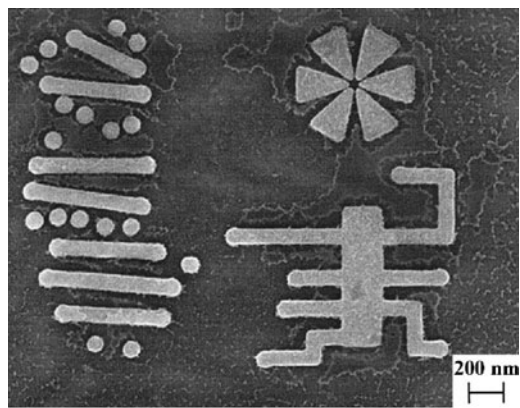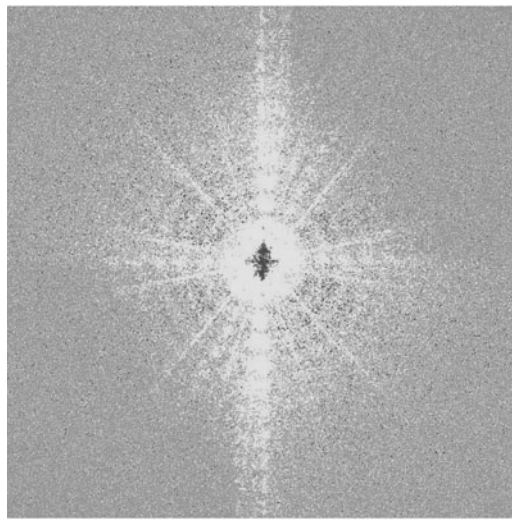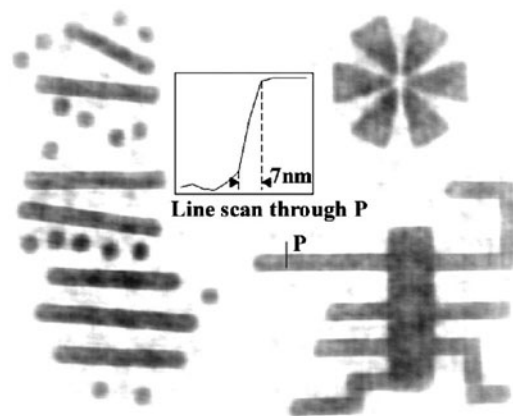
Figure 9. (a) A scanning electron microscopy picture of a 2D gold object. (b) An x-ray diffraction pattern of the object. (c) Reconstruction of the object from its diffraction pattern. From [61].
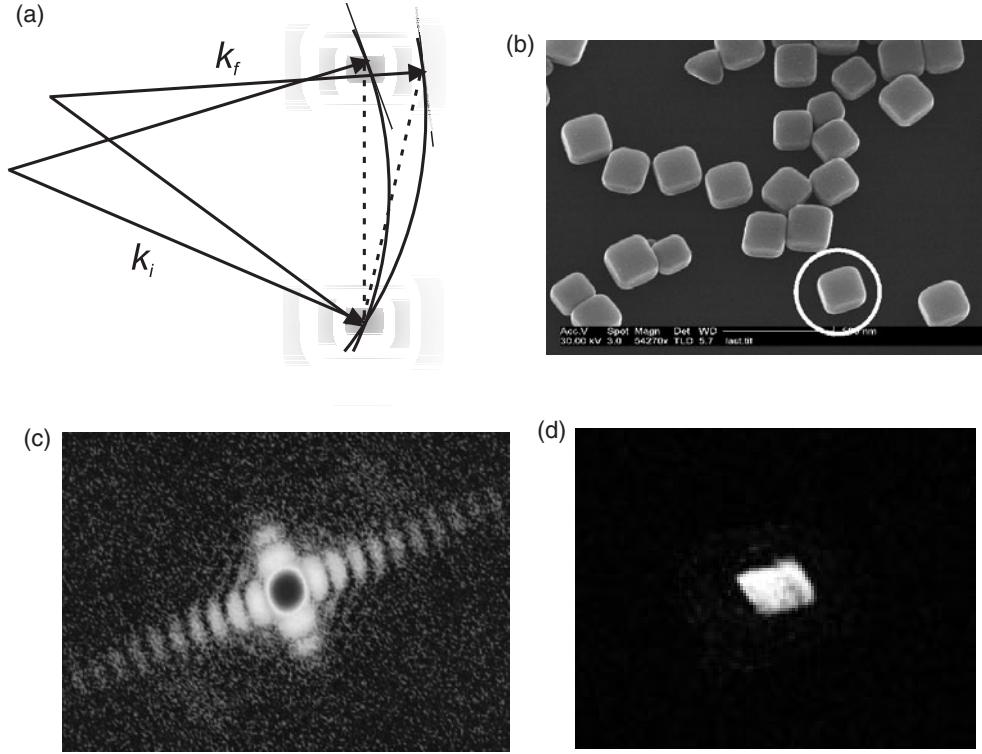
Figure 10. (a) The reciprocal-space geometry for diffraction from the lattice planes of a nanocube. (b) A scanning electron microscopy picture of a collection of Ag nanocubes of size 160 nm. (c) An x-ray diffraction pattern of a nanocube. (d) Reconstruction of the nanocube from its diffraction pattern. From [74].

is chosen to be much larger than two. If we denote the oversampling ratio along a particular direction transverse to the beam direction by $\mathcal{O}$, the criterion for the beam divergence along that direction reads

$$\Delta\theta < \frac{\lambda}{\mathcal{O}a}. \tag{34}$$

We conclude that the transverse coherence length must exceed the object size by as much as the oversampling factor: $\xi_t > a\mathcal{O}$. Similarly, the criterion on the bandwidth of the source, given in (9), has to be modified:

$$\frac{\Delta\lambda}{\lambda} < \frac{s}{\mathcal{O}a}. \tag{35}$$

The longitudinal coherence length, given by (5), should be correspondingly larger as well: $\xi_l > \lambda a\mathcal{O}/(2s)$, with s the desired spatial resolution.

Despite the oversampling, the requirements on the beam coherence can in most cases be readily met. That is, the more interesting applications of diffractive imaging are to be found in nanoscience. The smaller the object size a, the smaller the coherence length is allowed to be. For example, for the imaging of the 160 nm nanocubes in figure 10 with an oversampling factor of 10, the minimum transverse coherence length required is only 1.6 μm. By comparison, the transverse vertical coherence length for an unfocused beam from an undulator of a third-generation source is typically in the range 25–100 μm. Hence, one can accept a substantial
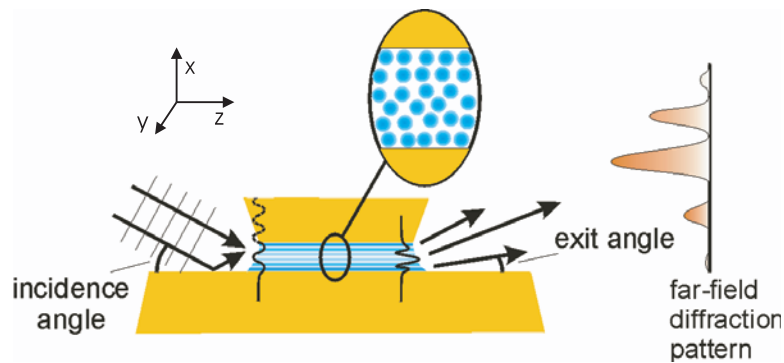
Figure 11. Waveguiding analysis of the structure of a confined colloid. The Fraunhofer diffraction pattern in the (x, z)-plane exhibits speckles in directions characteristic of the fluid's density profile across the gap. The figure is not drawn to scale: the gap size a is typically a few hundred nanometres, the length of confining geometry along the propagation direction of the beam is a few millimetres and the angles of incidence and exit, θ_i and θ_e, are less than the critical angle for total internal reflection ($<0.1°$). From [78].

decrease in ξ_v before the loss of coherence becomes noticeable. This opens the possibility of focusing the beam onto the nano-object. If the optics demagnifies the source by a factor M, ξ_v decreases by the same factor. Beam compression by a factor of 15–60 in the vertical direction is therefore possible without compromising the measurement [75]. In the horizontal direction, along which the coherence length is typically a factor of ten smaller, the demagnification factor should be chosen correspondingly smaller. For small a, the requirement on the longitudinal coherence length, i.e. on the monochromator bandwidth, is relaxed as well, resulting in an additional flux gain. In all, a total flux gain of a few orders of magnitude is possible. This example shows the importance of matching the transverse and longitudinal coherence lengths to the dimensions of the object and to the oversampling factor.

8. A special case: fluid confined in one dimension

The conditions for object reconstruction, as discussed in section 6, are not always fulfilled. Let us consider, for example, the object depicted in figure 11. A colloidal fluid is confined by two parallel plates, providing a model for a lubricated contact between two surfaces [76]. X-ray scattering from the confined fluid is employed in order to address the question of whether the colloidal particles order in layers parallel to the confining surfaces [77, 78], as has indeed been predicted [79, 80]. The gap between the surfaces is in the range of a few hundred nanometres. Hence, the object size a along the confining direction x is less than a typical vertical coherence length, and scattering within the (x, z)-plane is a coherent process. By contrast, scattering within the infinitely extended plane of confinement, the (y, z)-plane, is incoherent. One may question whether it is possible to uniquely reconstruct from the far-field diffraction pattern in the (x, z)-plane the density profile of the fluid along the x-direction. The answer appears to be *no*. The one-dimensional nature of the problem implies that different field profiles across the exit of the gap may yield the same diffraction pattern, irrespective of the degree of oversampling [68]. Since the emerging field profile is a fingerprint of the fluid's density profile, it therefore appears that the latter cannot be obtained by direct inversion of the diffraction pattern, when no additional assumptions about the system are made.

The fluid's density profile, as expressed by the spatially varying refractive index $n(x, z)$, is in this case determined by trial and error [77]. The experiment was conducted as follows:
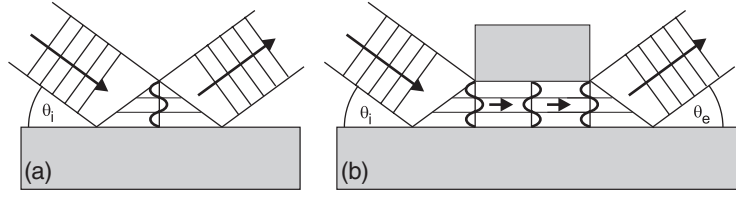
Figure 12. (a) A plane wave incident under a glancing angle θ_i is reflected from a surface. The spacing between two consecutive nodes of the standing wavefield equals $\lambda/(2\theta_i)$, in the small-angle approximation. (b) The upper surface of the waveguide is positioned at a node of the standing wavefield. The wavefield then becomes a pure mode of the resulting parallel-plate waveguide. For $\theta_i = \theta_m$, mode m is excited. The spacing a between the plates then equals $(m + 1)$ times the internodal spacing $\lambda/(2\theta_m)$. The displayed mode is TE$_2$ ($m = 2$). Here, the wavefield within the material of the confining plates is considered to be negligibly small. From [83].

in order to suppress the scattering from the confining plates, the angle of incidence θ_i of the beam is chosen to be smaller than the critical angle for total reflection from the lower surface. Interference between the incident beam and the reflected beam then gives rise to a standing wave pattern at the gap entrance. If the upper surface is positioned at a node of the standing wavefield, the wave is captured within the space between the plates, and the parallel-plate geometry becomes a waveguide for this particular mode (see also figure 12). For example, the mode shown in figures 11 and 12 at the gap entrance is the transverse electric mode TE$_2$, having two nodes between the plates. Variations in $n(x, z)$ within the gap cause the wavefront belonging to one particular mode to scatter into other modes of the waveguide. The total wavefield, which is a superposition of the discrete modes, therefore differs at the exit from that at the entrance (see figure 11). How does one deduce $n(x, z)$ from the changes in the wavefield? Our confined system is a *thick phase object* [78], so the approximation (17) leading to the single-scattering (kinematic) diffraction formulae (18) and (19) cannot be made. Instead one must go back a few steps and solve the Helmholtz equation [2]

$$\nabla^2 \Psi + k^2 n^2(x, z)\Psi = 0, \tag{36}$$

where $\nabla^2 = \partial^2/\partial x^2 + \partial^2/\partial z^2$ and $\Psi(x, z) = E_y(x, z)$, with E_y the transverse electric field. Solutions of (36) can be readily found for the case where the refractive index of the confined fluid only depends on x, which for the parallel-plate geometry of figure 11 is a reasonable assumption. The *ansatz*

$$\Psi(x, z) = \phi(x)\exp(-i\beta z) \tag{37}$$

leads to the homogeneous second-order differential equation

$$\frac{d^2\phi}{dx^2} + [k^2 n(x)^2 - \beta^2]\phi = 0. \tag{38}$$

Solutions to this equation should fulfil the boundary conditions, namely that both ϕ and $d\phi/dx$ are continuous across the fluid–solid interfaces. The parameter β in (37), called the *propagation factor*, is the component of the wavevector along the direction of propagation.

Let us first assume that there is *no fluid* between the confining surfaces, i.e., $n(x) = 1$ for $0 \leqslant x < a$, $n(x) = n = 1 - \delta$ for $x < 0$ and $x \geqslant a$ [81]. It is then readily verified that the solutions of (38) are of the form

$$\phi_e(x) = \begin{cases} A\cos(k_x a/2)\exp(\gamma x), & x < 0, \\ A\cos[k_x(x - a/2)], & 0 \leqslant x < a, \\ A\cos(k_x a/2)\exp[-\gamma(x - a)], & x \geqslant a, \end{cases} \tag{39}$$

or

$$\phi_{o}(x) = \begin{cases} -A \sin (k_x a/2) \exp(\gamma x), & x < 0, \\ A \sin [k_x (x - a/2)], & 0 \leqslant x < a, \\ A \sin (k_x a/2) \exp[-\gamma (x - a)], & x \geqslant a, \end{cases} \qquad (40)$$

where $\gamma = (\beta^2 - n^2 k^2)^{1/2}$ and $k_x = (k^2 - \beta^2)^{1/2}$, and where ϕ_e and ϕ_o are respectively *even* and *odd* with respect to the mid-plane of the waveguide. A is a normalization constant for the wavefunctions. The boundary conditions on ϕ_e are fulfilled if

$$k_x \tan\left(\frac{k_x a}{2}\right) = \gamma \qquad (41)$$

and those on ϕ_o if

$$k_x \cot\left(\frac{k_x a}{2}\right) = -\gamma. \qquad (42)$$

The transcendental equations (41) and (42) can be solved numerically for β, and the different solutions correspond to the waveguide modes. The solutions take a particularly simple form for $\gamma \rightarrow \infty$, which is the limit of negligible penetration of the evanescent wavefunction into the confining material. In this case, (41) and (42) yield the conditions $k_x a = (2l + 1)\pi$ and $k_x a = 2l\pi$ for the even and odd modes respectively, with l an integer. It is easily verified that the corresponding wavefunctions within the guiding medium are of the form $\phi_e = A \sin[(2l + 1)\pi x/a]$ and $\phi_o = A \sin(2l\pi x/a)$. It is convenient [82] to label these modes instead with the index $m = 0, 1, 2, \ldots$ and to rewrite them as

$$\phi_m(x) = \sqrt{\frac{2}{a}} \sin\left(\frac{k\theta_m x}{a}\right), \qquad (43)$$

where the so-called *mode angle* θ_m is defined by

$$\theta_m \equiv \frac{(m + 1)\pi}{ka} = \frac{\lambda(m + 1)}{2a}, \qquad (44)$$

and the pre-factor $A = \sqrt{2/a}$ is chosen such that the $\{\phi_m\}$ are properly normalized:

$$\int_0^a |\phi_m(x)|^2 \, dx = 1. \qquad (45)$$

The $\{\phi_m\}$ form a orthonormal basis set, i.e.

$$\langle m|n \rangle \equiv \int_0^a \phi_m^*(x) \, \phi_n(x) \, dx = \delta_{mn}, \qquad (46)$$

where δ_{mn} is the Kronecker delta, and the bra–ket notation has been introduced. With this convention of mode labelling, the even modes TE_m correspond to even m and the odd modes to odd m. The wavefield can be expressed as a linear combination of modes:

$$|\Psi\rangle = \sum_m \langle m|\Psi \rangle |m\rangle, \qquad (47)$$

which in the coordinate representation is given by

$$\langle x, z|\Psi \rangle = \sum_m c_m \exp(-i\beta_m z) \, \phi_m(x). \qquad (48)$$

The coefficients $\{c_i\}$ are determined by the wavefield at the gap entrance. If the incidence angle θ_i equals a mode angle θ_n, the standing wave at the gap entrance matches that of the waveguide mode TE_n exactly (to within the approximation that the evanescent fields are negligibly small; see also figure 12). In this case all $\{c_i\}$ except c_n are zero, and mode n emerges undisturbed at the

waveguide exit, after which it is reflected from the lower surface at an exit angle $\theta_e = \theta_n = \theta_i$. For a general angle of incidence θ_i, which may differ from a mode angle, the decomposition into waveguide modes can now be readily found. The standing wavefield at the entrance is of the form

$$\langle x, 0|\Psi\rangle_{in} = \sqrt{\frac{2}{a}} \sin(k\theta_i x), \tag{49}$$

and the relative amplitude c_m of mode m is given by

$$c_m(\theta_i) = \langle m|\Psi\rangle_{in} = \int_x \langle m|x, 0\rangle\langle x, 0|\Psi\rangle_{in}$$

$$= \frac{2}{a} \int_0^a \sin(k\theta_m x) \sin(k\theta_i x) \,dx = \frac{2(-1)^m}{ka} \frac{\theta_m \sin(k\theta_i a)}{\theta_m^2 - \theta_i^2}. \tag{50}$$

Note that $c_m(\theta_n) = \delta_{mn}$. The wavefield after propagation over a distance L is given by (47) and (48), with $z = L$ and the relative mode amplitudes given by (50). For diffraction into the detector at exit angle θ_e, the standing wavefield at the waveguide exit must have the form

$$\langle x, L|\Psi\rangle_{out} = \sqrt{\frac{2}{a}} \sin(k\theta_e x), \tag{51}$$

in analogy with (49). The intensity $I(\theta_i, \theta_e)$ diffracted into angle θ_e is then obtained by projecting the wavefunction $|\Psi\rangle$ at the waveguide exit onto the wavefield $|\Psi\rangle_{out}$:

$$I(\theta_i, \theta_e) = |_{out}\langle\Psi|\Psi\rangle|^2 = \left| \int_x {}_{out}\langle\Psi|x, L\rangle\langle x, L|\Psi\rangle \right|^2$$

$$= \left| \frac{2}{a} \sum_m c_m(\theta_i) \exp(-i\beta_m L) \int_0^a \sin(k\theta_m x) \sin(k\theta_e x) \,dx \right|^2$$

$$= \left| \sum_m \exp(-i\beta_m L) c_m(\theta_i) c_m(\theta_e) \right|^2, \tag{52}$$

The intensities $I(\theta_i, \theta_e)$ calculated with (52) are in excellent agreement with the measured values (see figure 13). Contour plots of $I(\theta_i, \theta_e)$ exhibit a sequence of strong maxima along the diagonal at the positions of the mode angles, in accord with the relation $I(\theta_m, \theta_n) = \delta_{mn}$. The characteristic beating in the intensity maxima and minima along the diagonal arises from the mode-dependent phase factors $\exp(-i\beta_m L)$ in (52), i.e. from multi-mode interference. One single contour plot represents a collection of diffraction patterns taken at different object rotation angles θ_i, in analogy with the tomograms discussed earlier. Hence, data are available in two dimensions, and it is an interesting—though in this case a somewhat academic—question whether the object can be reconstructed from the contour plot without any pre-knowledge.

We now consider the presence of a *layered fluid* (colloid) between the confining surfaces [77]. The layering is modelled through a periodically varying refractive index of the form

$$n(x) = 1 - \sum_{n=0}^{N} a_n \cos\left(\frac{2\pi n x}{a}\right). \tag{53}$$

The differential equation (38) with this functional form of the coefficients is known as Hill's equation [85], and periodic solutions can be constructed with the use of Floquet's theorem. If the layering profile contains a single spatial frequency, we have the special case

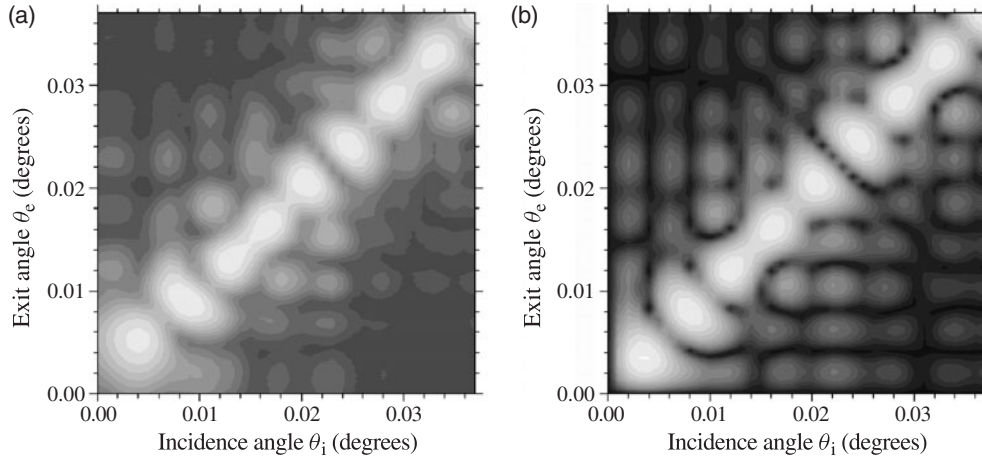$$n(x) = 1 - a_0 - a_1 \cos\left(\frac{2\pi l x}{a}\right), \tag{54}$$

Figure 13. Logarithmic contour plots of the intensity diffracted from the exit of a planar waveguide with an extended lower plate, as a function of θ_i and θ_e. The x-ray wavelength $\lambda = 0.0930$ nm and the waveguide length $L = 4.85$ mm. (a) The measured intensity distribution for a waveguide with SiO_2 plates at a distance $a = 650$ nm. (b) The intensity distribution calculated with (52) for the same plate distance. From [84].

where $1 - a_0$ is the spatially averaged refractive index of the fluid, and the cosine term describes a modulation in the refractive index associated with l layers. The corresponding solutions of (38) are the Matthieu functions, which for specific values of β are periodic and fulfil the relevant boundary conditions. The Matthieu functions are the fundamental waveguide modes belonging to this specific layering profile, and they form an orthogonal basis set in just the same way as the sine functions in (43) represent the modes for the waveguide without layered fluid. Nonetheless, expressing the general solution as a linear combination of empty-waveguide (i.e. sine) modes provides more insight. Within the latter representation, the layered profile causes intermodal scattering. For example, it turns out that a profile of l layers will cause scattering of an empty-waveguide mode m into the modes $m - 2l$, $m + 2l$ and $2l - m - 2$. In plots such as figure 13, additional intensity maxima are then found along co-diagonals displaced by $\pm 2l$ with respect to the main diagonal. In addition, a cross-diagonal intersects the main diagonal at $\theta_i = \theta_{pl-1}$, with $p = 1, 2, \ldots$.

Instead of solving Hill's equation, one may also find the wavefield by use of the *beam propagation method*. This numerical method allows for a refractive index profile that is also z-dependent, and in general it puts no restrictions on the form of $n(x, z)$. One substitutes

$$\Psi(x, z) = \psi(x, z) \exp(-i\tilde{\beta}z) \tag{55}$$

into (36), which removes the rapid variations in the field. The constant $\tilde{\beta}$ is the reference propagation constant and denotes a representative value of $kn(x, z)$. One may use $\tilde{\beta} = k$ since $n(x, z) \approx 1$. Now, if the $\partial^2\psi/\partial z^2$ term is neglected, one obtains

$$\frac{\partial \psi}{\partial z} = \frac{i}{2k}\left\{-\frac{\partial^2\psi}{\partial x^2} - k^2\left[n^2(x, z) - 1\right]\psi\right\}. \tag{56}$$

The beam is propagated by numerical integration of (56); given $\psi(x, z)$ one calculates $\psi(x, z + \Delta z)$. This may be achieved using different numerical schemes [86, 87]. By neglecting the $\partial^2\psi/\partial z^2$ term, we make the so-called *parabolic approximation* [87]. This is justified whenever the variations in the refractive index are small, i.e. $\Delta n/n \ll 1$, and the scattering is in the near-forward direction, i.e. $k_x/k \ll 1$. Both conditions are easily met for x-rays.
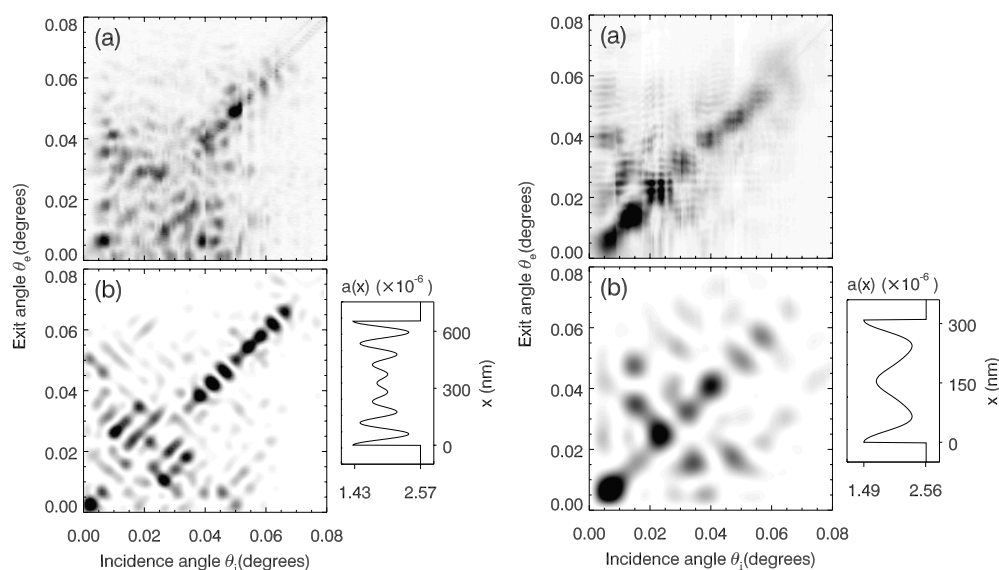
Figure 14. Left: contour plots of the diffracted intensity $I(\theta_i, \theta_e)$, (a) measured for a colloid confined within a gap of 655 nm width, (b) calculated for the refractive index profile $n(x) = 1 - a(x)$ shown. Right: (a) and (b): as in (a) and (b) on the left, but for a gap of 310 nm width. The colloid is a 10 vol% suspension of 110 nm diameter SiO_2 spheres in dimethylformamide. From [77].

Examples of waveguiding within a confined colloid are shown in figure 14 (see also [77]). The colloid, consisting of a 10 vol% suspension of 110 nm diameter SiO_2 spheres in dimethylformamide, was confined between two SiO_2 plates of 4.85 mm diameter, positioned at separations of 655 and 310 nm. Intense off-diagonal maxima are observed, indicative of strong intermodal coupling. For a gap of 655 nm (figure 14, left panel (a)), a diffuse cross-diagonal is visible that intersects the main diagonal at a mode angle $\sim\theta_5$. This indicates the presence of six layers ($l \sim 6$). At a gap of 310 nm (figure 14, right panel (a)), only two layers are present. If the refractive index profile were to be z-independent, the main diagonal in the contour plot $I(\theta_i, \theta_e)$ would be a symmetry line. The off-diagonal features are clearly asymmetric, signifying that this assumption for the refractive index profile cannot be made. Reasonable fits to the measured contour plots are obtained for the displayed $n(x)$ profiles, provided that they are asymmetrically positioned within the intervals $1.81 < z < 3.85$ and $1.90 < z < 3.33$ mm for the 655 and 310 nm gaps, respectively. The best-fit profiles show that the confinement induces a strong layering of the particles in a close-packed structure, whose order decays with increasing distance from the surfaces. This, as well as the non-uniformity of the ordered regions within the plane of the gap, strongly suggests that the confinement induces a *crystallization* of the colloid at volume densities much lower than the critical density for crystallization of bulk colloid [88].

The intensity peaks in $I(\theta_i, \theta_e)$ can be viewed as speckles, in the sense that they reflect the largest length scale within the finite-size object, which is the gap width a. Their angular width and spacing equal $\lambda/2a$. As in the previous applications of coherent scattering, one observes a particular realization of the system instead of an ensemble average. For the 1D example discussed here, there occurs some averaging within the (y, z)-plane, but one should not be surprised that it is difficult to reproduce all of the observed diffraction features with a model. Finding the correct model by trial and error would require an unrealistically long search in

multi-parameter space, and here one would benefit from a direct inversion. But then one has to modify the geometry either into a 2D one or to provide a reference beam for interference, as in holography. An added complication is that waveguiding, by its very nature, operates in the limit of *thick* phase objects.

The spatial resolution in $n(x, z)$ that can be achieved with the waveguiding technique is determined by the critical angle for total internal reflection θ_c. The guided mode with the highest mode number is that at a mode angle just below θ_c; all higher modes will radiate out of the waveguide. The spacing between two nodes in the standing wave of the highest guided mode is $\sim \lambda/2\theta_c$ and, without any additional knowledge about the system, it is impossible to resolve features at a distance scale smaller than, say, half this internodal spacing. Hence, the resolution is of the order $s \sim \lambda/4\theta_c$. We note that [4]

$$\theta_c = \sqrt{2\delta} = \lambda\sqrt{r_e \Delta n_e/\pi}, \tag{57}$$

where use has been made of (12), and Δn_e represents the difference in electron density across the interface. Since θ_c scales with λ, the resolution s is independent of λ. For, e.g., the silica–water interface, we find $s \sim 15$ nm. This resolution is adequate for the structure determination of e.g. colloids and many other objects, but is insufficient for studies of ordering phenomena on the molecular scale. For the latter, much larger scattering angles (momentum transfer values) are required, bringing us well outside of the waveguiding regime and back into the kinematic diffraction regime.

9. Outlook

As synchrotron radiation sources become more brilliant and more stable, the number of applications of coherent x-ray scattering will continue to grow. There are interesting developments not only in the areas of diffractive imaging and waveguiding, but also in holography, microscopy and intensity correlation spectroscopy. What are the challenges in these areas?

One of the main challenges in *coherent diffractive imaging* is to improve the resolution. Since no optical elements are involved, the spatial resolution of the method is not limited by a small numerical aperture or by aberrations. Recording coherent diffraction patterns over a wide range of momentum transfer could in theory yield a resolution as good as 0.1 nm, but in practice a trade-off has to be made with the counting rate and with possible radiation damage occurring at high beam doses. To date, a resolution of 7 nm has been achieved (see [61] and section 7). For biological specimens, the ultimate resolution will be entirely determined by their resistance to high radiation doses, and it has been estimated that 5 nm would be realistic [66]. Compared with what can be achieved with cryo-electron microscopy, this is a modest number. However, x-ray scattering is more element-specific, and the depth of field is in the micrometre range, i.e. in the range of cell dimensions. By contrast, high-resolution transmission electron microscopy requires much thinner samples and more involved sample preparation.

Coherent resonant magnetic scattering in the soft x-ray range shows great promise as a technique for the diffractive imaging of magnetic domains in thin films. *Magnetic speckle patterns* have been reported in [51] and [65]. Inversion of these patterns into real-space magnetic structures has yet to be carried out. Another challenge will be to perform such studies in the time domain with picosecond resolution.

Holographic techniques with a reference beam have recently been extended to the hard x-ray region. Images of micrometre-sized test objects were obtained using Fourier transform holography, for which the reference source is in the plane of the object [89]. Holography is

also possible using atoms in a crystal lattice as the source or the detector [90]. This technique, which provides atomic resolution in extended crystals, falls outside the scope of this paper, because it does not need a coherent beam, i.e., a beam with a coherence length larger than a few interatomic distances. Clearly, all these techniques are only at the beginning of their development, and their application will be extended to nanometre-scale objects or crystals as more brilliance becomes available.

The waveguides discussed in section 8 can be converted into focusing devices. By simply tilting the upper surface of the waveguide shown in figure 12, one obtains a wedge [91]. In such a tapered device, the standing wavefield becomes compressed, and it has been shown theoretically that the lowest mode TE_0 at the entrance can be compressed to a height $\sim 0.7 \times \lambda/(2\theta_c)$ [92]. Because of (57), the minimum height is only a property of the material and the geometry. For a planar wedge of SiO_2 with an air gap, we predict a line focus of 13 nm height, and for confining materials of higher Z-number, a focus height below 10 nm is possible. Similar limits should apply to two dimensions, to be achieved either with the use of a hollow tapered glass capillary [93] or with a circular zone plate having an outer zone of correspondingly small width. Such spot sizes are not yet available in the hard x-ray regime, but in the soft x-ray regime one is getting close (~ 20 nm; see [94]). The first 2D x-ray waveguides have recently been reported and a beam of 70 nm $\times$ 30 nm cross section has been extracted [95]. Here, the beam was coupled into a hollow rectangular structure by use of a resonant beam coupling technique. Future devices may be tapered, and instead of resonant beam coupling, one may consider pre-focusing of the beam onto the waveguide entrance. The most important applications for such focusing devices are to be found in scanning microscopy and imaging.

X-ray intensity correlation spectroscopy (XPCS), which is particularly suited for studies of the dynamics of soft condensed matter [14], requires an extremely high photon flux, and the accessible range of momentum transfers is therefore limited by the counting rate. This technique would be revolutionized if more advanced position-sensitive detectors were available. Pixel detectors, which are at present being developed for structural biology [96], are very promising. Each pixel is a Si pn-junction having its own read-out on a chip that contains for each pixel an amplifier, pulse shaper and counter [97]. These single-photon counting detectors may enable energy and time stamping of events and cross-correlation of pixels in the spatial and temporal domains.

With the advent of x-ray free electron lasers (FELs) in six to eight years from now, we will be confronted with completely different conditions for coherent scattering experiments [98]; the FELs will produce transversely coherent beams at 10^{10} times higher brilliance than third-generation synchrotron radiation sources and generate pulses in the femtosecond range. This opens up completely new avenues of research. However, photon fluxes at FELs will also be so large that radiation damage will be an important issue. Damage effects will be forbiddingly high in *biomaterials*. For this reason it has been proposed that, e.g., diffraction experiments on single biomolecules be carried out within a single photon pulse. On such a short timescale (e.g., 20 fs) the diffraction pattern is recorded before the molecule flies apart as a result of the Coulomb explosion following photon-induced ionization [99]. This issue needs further investigation.

References

[1] Lengeler B 2001 *Naturwissenschaften* **88** 249–60
[2] Born M and Wolf E 1980 *Principles of Optics* (Oxford: Pergamon)
[3] Goodman J W 1985 *Statistical Optics* (New York: Wiley)
[4] Als-Nielsen J and McMorrow D 2001 *Elements of Modern X-Ray Physics* (New York: Wiley)
[5] Sinha S K, Tolan M and Gibaud A 1998 *Phys. Rev.* B **57** 2740–53
[6] Berne B J and Pecora R 2000 *Dynamic Light Scattering* (Toronto: General Publishing Company, Ltd)
[7] Pusey P N 1977 Photon correlation spectroscopy and velocimetry *Statistical Properties of Scattered Radiation* (*NATO Advanced Study Institutes Series*) ed H Z Cummins and E R Pike (Amsterdam: Elsevier)
[8] Dierker S B, Pindak R, Fleming R M, Robinson I K and Berman L 1995 *Phys. Rev. Lett.* **75** 449–52
[9] Mochrie S G J, Mayes A M, Sandy A R, Sutton M, Brauer S, Stephenson G B, Abernathy D L and Grübel G 1997 *Phys. Rev. Lett.* **78** 1275–8
[10] Thurn-Albrecht T *et al* 1999 *Phys. Rev.* E **59** 642–8
[11] Riese D O 2000 Fluid dynamics in charge stabilized colloidal suspensions *PhD Thesis* University of Amsterdam
[12] Fera A, Dolbnya I P, Grübel G, Muller H G, Ostrovski B I, Shalaginov A N and de Jeu W H 2000 *Phys. Rev. Lett.* **85** 2316–9
[13] Lurio L B *et al* 2000 *Phys. Rev. Lett.* **84** 785–8
[14] Grübel G, Abernathy D L, Riese D O, Vos W and Wegdam G H 2000 *J. Appl. Crystallogr.* **33** 424–7
[15] Abernathy D L, Grübel G, Brauer S, McNulty I, Stephenson G B, Mochrie S G J, Sandy A R, Mulders N and Sutton M 1998 *J. Synchrotron Radiat.* **5** 37–47
[16] Sandy A R, Lurio L B, Mochrie S G J, Malik A, Stephenson G B, Pelletier J F and Sutton M 1999 *J. Synchrotron Radiat.* **6** 1174–84
[17] Takayama Y, Tai R Z, Hatano T, Miyahara T, Okamoto W and Kagoshima Y 1998 *J. Synchrotron Radiat.* **5** 456–8
[18] Bartels R A, Paul A, Green H, Kapteyn H C, Murname M M, Backus S, Christov I P, Liu Yanwei, Attwood D and Jacobsen C 2002 *Science* **297** 376–8
[19] Vlieg E, de Vries S A, Alvarez J and Ferrer S 1997 *J. Synchrotron Radiat.* **4** 210–3
[20] Bongaerts J H H, David C, Drakopoulos M, Zwanenburg M J, Wegdam G H, Lackner T, Keymeulen H and van der Veen J F 2002 *J. Synchrotron Radiat.* **9** 383–93
[21] Kohn V, Snigireva I and Snigirev A 2000 *Phys. Rev. Lett.* **85** 2745
[22] See, e.g., http://www-cxro.lbl.gov
[23] Hwu Y, Tsai W-L, Groso A, Margaritondo G and Je Jung Ho 2003 *J. Phys. D: Appl. Phys.* **35** R105–19
[24] Raven C, Snigirev A, Snigireva I, Spanne P, Souvorov A and Kohn 1996 *Appl. Phys. Lett.* **69** 1–3
[25] Kohn V, Snigireva I and Snigirev A 2001 *Opt. Commun.* **198** 293–309
[26] Stampanoni M F M 2003 *PhD Thesis* ETH-Zürich
[27] Kak A C and Slaney M 1987 *Principle of Computerized Tomographic Imaging* vol 69 (New York: IEEE) http://www.slaney.org/pct/index.html
[28] Sutton M, Mochrie S G J, Greytak T, Nagler S E, Berman L E, Held G A and Stephenson G B 1991 *Nature* **352** 608–10
[29] Cai Z H, Yun W B, McNulty I, Huang K G and Russell T P 1994 *Phys. Rev. Lett.* **73** 82–5
[30] Robinson I K, Pindak R, Fleming R M, Dierker S B, Ploog K, Grübel G, Abernathy D L and Als-Nielsen J 1995 *Phys. Rev.* B **52** 9917–24
[31] Libbert J L, Pindak R, Dierker S B and Robinson I K 1997 *Phys. Rev.* B **56** 6454–7
[32] Robinson I K, Pitney J A, Libbert J L and Vartanyants I A 1998 *Physica* B **248** 387–94
[33] Pitney J A, Robinson I K, Vartanyants I A, Appleton R and Flynn C P 2000 *Phys. Rev.* B **62** 13084
[34] Retsch C C and McNulty I 2001 *Phys. Rev. Lett.* **87** 77401
[35] Cowley J M 1995 *Diffraction Physics* 3rd edn (Amsterdam: North-Holland)
[36] Sayre D 1952 *Acta Crystallogr.* **5** 843
[37] Gerchberg R W and Saxton W O 1972 *Optik* **35** 237–46
[38] Fienup J R 1978 *Opt. Lett.* **3** 27–9
[39] Bates R H T 1982 *Optik* **61** 247–62
[40] Fienup J R 1982 *Appl. Opt.* **21** 2758
[41] Fienup J R 1986 *J. Opt. Soc. Am.* **3** 284–8

[42] Fienup J R 1987 *J. Opt. Soc. Am.* **4** 118–23
[43] Vartanyants I A, Pitney J A, Libbert J L and Robinson I K 1997 *Phys. Rev.* B **55** 13193–201
[44] Miao J, Sayre D and Chapman H N 1998 *J. Opt. Soc. Am.* **15** 1662–9
[45] Robinson I K, Libbert J L, Vartanyants I A, Pitney J A, Smilgies D M, Abernathy D L and Grübel G 1999 *Phys. Rev.* B **60** 9965–72
[46] Pitney J A and Vartanyants I A 1999 *Proc. SPIE* **3815** 199–207
[47] Miao J and Sayre D 2000 *Acta Crystallogr.* A **56** 596–605
[48] Vartanyants I, Em C, Donner W and Dosch H 2000 *Appl. Phys. Lett.* **77** 3929–31
[49] Miao J, Kirz J and Sayre D 2000 *Acta Crystallogr.* D **56** 1312–5
[50] Miao J, Hodgson K O and Sayre D 2001 *Proc. Natl Acad. Sci.* **98** 6641–5
[51] Peters J F, de Vries M A, Miguel J, Toulemonde O and Goedkoop J B 2000 *ESRF Newslett.* **34** 15–6
[52] Robinson I K and Vartanyants I A 2001 *Appl. Surf. Sci.* **182** 186–91
[53] Robinson I K, Vartanyants I A, Williams G J, Pfeiffer M A and Pitney J A 2001 *Phys. Rev. Lett.* **87** 195505
[54] Vartanyants I A and Robinson I K 2001 *J. Phys.: Condens. Matter* **13** 10593–611
[55] Spence J C, Howells M, Marks L D and Miao J 2001 *Ultramicroscopy* **90** 1–6
[56] Miao J, Ishikawa T, Johnson B, Anderson E H, Lai B and Hodgson K O 2002 *Phys. Rev. Lett.* **89** 088303
[57] Mentes T O, Sanchez C and Kao C C 2002 *J. Synchrotron Radiat.* **9** 90–5
[58] Vartanyants I A and Robinson I K 2001 *Appl. Surf. Sci.* **182** 186–91
[59] Vartanyants I A and Robinson I K 2003 *J. Synchrotron Radiat.* **10** 409–15
[60] He H, Marchesini S, Howells M, Weierstall U, Hembree G and Spence J C H 2003 *Acta Crystallogr.* A **59** 143–52
[61] Miao J, Ishikawa T, Anderson E H and Hodgson K O 2003 *Phys. Rev.* B **67** 174104
[62] Miao J, Amonette J E, Nishino Y, Ishikawa T and Hodgson K O 2003 *Phys. Rev.* B **68** 012201
[63] Miao J, Hodgson K O, Ishikawa T, Larabell C, LeGros M and Nishino Y 2003 *Proc. Natl Acad. Sci.* **100** 110–2
[64] Williams G J, Pfeiffer M A, Vartanyants I A and Robinson I K 2003 *Phys. Rev. Lett.* **90** 175501
[65] Eisebitt S, Lorgen M, Eberhardt W, Lüning J, Stoöhr J, Rettner C T, Hellwig O, Fullerton E E and Denbeaux G 2003 *Phys. Rev.* B **68** 104419
[66] Marchesini S *et al* 2004 *Proc. 8th Int. Conf. on Synchrotron Radiation Instrumentation (San Francisco, CA, 2003) (AIP Series of Conference Proceedings)* at press
[67] Shannon C E 1949 *Proc. Inst. Radio Eng.* **37** 10–21
[68] Bruck Yu M and Sodin L G 1979 *Opt. Commun.* **30** 304–8
[69] Cloetens P, Ludwig W, Baruchel J, Van Dyck D, Van Landuyt J, Guigay J P and Schlenker M 1999 *Appl. Phys. Lett.* **75** 2912–4
[70] Nugent K A, Gureyev T E, Cookson D F, Paganin D and Barnea Z 1996 *Phys. Rev. Lett.* **77** 2961–4
[71] Coene W, Janssen G, Op de Beeck M and Van Dyck D 1992 *Phys. Rev. Lett.* **69** 3743–6
[72] Teague M R 1983 *J. Opt. Soc. Am.* **73** 1434–41
[73] Miao J, Charalambous P, Kirz J and Sayre D 1999 *Nature* **400** 342–4
[74] Pfeiffer F and Robinson I K 2004 at press
[75] Robinson I K, Pfeiffer F, Vartanyants I A, Sun Y and Xia Y 2003 *Opt. Express* **11** 2329–34
[76] Persson B N J 1998 *Sliding Friction* (Berlin: Springer)
[77] Zwanenburg M J, Bongaerts J H H, Peters J F, Riese D O and van der Veen J F 2000 *Phys. Rev. Lett.* **85** 5154–7
[78] Zwanenburg M J 2001 X-ray waveguiding studies of ordering phenomena in confined fluids *PhD Thesis* University of Amsterdam
[79] Bushan B, Israelachvili J N and Landman U 1995 *Nature* **374** 607
[80] Israelachvili J 1992 *J. Vac. Sci. Technol.* A **10** 2961
[81] Zwanenburg M J, Peters J F, Bongaerts J H H, de Vries S A, Abernathy D L and van der Veen J F 1999 *Phys. Rev. Lett.* **82** 1696–9
[82] Marcuse D 1991 *Theory of Dielectric Waveguides* (San Diego, CA: Academic)
[83] Bongaerts J H H 2003 Coherent light and x-ray scattering studies of the dynamics of colloids in confinement *PhD Thesis* University of Amsterdam
[84] Zwanenburg M J, Ficke H G, Neerings H and van der Veen J F 2000 *Rev. Sci. Instrum.* **71** 1723–32
[85] Magnus W and Winkler S 1966 *Hill's Equation (Interscience Tracts in Pure and Applied Mathematics, No. 20)* (New York: Wiley)
[86] Maerz R 1994 *Integrated Optics: Design and Modeling* (Boston, MA: Artech House Publishers)
[87] Scarmozzino R and Osgood R M Jr 1991 *J. Opt. Soc. Am.* B **8** 724–31
[88] Pusey P N and van Megen W 1986 *Nature* **320** 340
[89] Leitenberger W and Snigirev A 2004 at press
[90] Faigel G and Tegze M 1999 *Rep. Prog. Phys.* **62** 355–93

[91] Zwanenburg M J, Bongaerts J H H, Peters J F, Riese D and van der Veen J F 2000 *Physica* B **283** 258–88

[92] Bergemann C, Keymeulen H and van der Veen J F 2003 *Phys. Rev. Lett.* **91** 204801

[93] Bilderback D H, Hoffman S A and Thiel D J 1994 *Science* **263** 201–3

[94] Chao W L, Denbeaux G P, Harteneck B, Liddle J A, Olynick D L, Pearson A L, Salmassi F, Song C Y and Attwood D T 2003 *Opt. Lett.* **28** 2019–21

[95] Pfeiffer F, David C, Burghammer M, Riekel C and Salditt T 2002 *Science* **297** 230–4

[96] Plaisier J R, Koning R I, Koerten H K, van Roon A M, Thomassen E A J, Kuil M E, Hendrix J, Broennimann C, Pannu N S and Abrahams J P 2003 *Nucl. Instrum. Methods* **509** 274–82

[97] Hülsen G *et al* 2004 *Proc. 8th Int. Conf. on Synchrotron Radiation Instrumentation (San Francisco, CA, 2003)* (*AIP Series of Conference Proceedings*) at press

[98] van der Veen J F 2004 *Proc. 8th Int. Conf. on Synchrotron Radiation Instrumentation (San Francisco, CA, 2003)* (*AIP Series of Conference Proceedings*) at press

[99] Neutze R, Wouters R, van der Spoel D, Weckert E and Hajdu J 2000 *Nature* **406** 752–7